frontiers in Cell and Developmental Biology

ORIGINAL RESEARCH
published: 10 December 2021
doi: 10.3389/fcell.2021.765673

Membrane Remodeling and Matrix Dispersal Intermediates During Mammalian Acrosomal Exocytosis

Miguel Ricardo Leung[1,2], *Ravi Teja Ravi*[1], *Bart M. Gadella*[3] *and Tzviya Zeev-Ben-Mordehai*[1,2]*

[1]Bijvoet Centre for Biomolecular Research, Utrecht University, Utrecht, Netherlands, [2]The Division of Structural Biology, Wellcome Centre for Human Genetics, The University of Oxford, Oxford, United Kingdom, [3]Department of Farm and Animal Health and Biomolecular Health Sciences, Faculty of Veterinary Medicine, Utrecht University, Utrecht, Netherlands

To become fertilization-competent, mammalian sperm must undergo a complex series of biochemical and morphological changes in the female reproductive tract. These changes, collectively called capacitation, culminate in the exocytosis of the acrosome, a large vesicle overlying the nucleus. Acrosomal exocytosis is not an all-or-nothing event but rather a regulated process in which vesicle cargo disperses gradually. However, the structural mechanisms underlying this controlled release remain undefined. In addition, unlike other exocytotic events, fusing membranes are shed as vesicles; the cell thus loses the entire anterior two-thirds of its plasma membrane and yet remains intact, while the remaining nonvesiculated plasma membrane becomes fusogenic. Precisely how cell integrity is maintained throughout this drastic vesiculation process is unclear, as is how it ultimately leads to the acquisition of fusion competence. Here, we use cryoelectron tomography to visualize these processes in unfixed, unstained, fully hydrated sperm. We show that paracrystalline structures within the acrosome disassemble during capacitation and acrosomal exocytosis, representing a plausible mechanism for gradual dispersal of the acrosomal matrix. We find that the architecture of the sperm head supports an atypical membrane fission–fusion pathway that maintains cell integrity. Finally, we detail how the acrosome reaction transforms both the micron-scale topography and the nanoscale protein landscape of the sperm surface, thus priming the sperm for fertilization.

Keywords: acrosome reaction, mammalian sperm, membrane fusion, cryo-elecron tomography, fertilization

OPEN ACCESS

Edited by:
Enrica Bianchi,
University of York, United Kingdom

Reviewed by:
Mariano G. Buffone,
CONICET Instituto de Biología y Medicina Experimental (IBYME), Argentina
María José Gómez-Torres,
University of Alicante, Spain

***Correspondence:**
Tzviya Zeev-Ben-Mordehai
z.zeev@uu.nl

Specialty section:
This article was submitted to Molecular and Cellular Reproduction, a section of the journal Frontiers in Cell and Developmental Biology

Received: *27 August 2021*
Accepted: *19 October 2021*
Published: *10 December 2021*

Citation:
Leung MR, Ravi RT, Gadella BM and Zeev-Ben-Mordehai T (2021) Membrane Remodeling and Matrix Dispersal Intermediates During Mammalian Acrosomal Exocytosis. Front. Cell Dev. Biol. 9:765673. doi: 10.3389/fcell.2021.765673

INTRODUCTION

Mammalian sperm must reside in the female reproductive tract for several hours before they are able to fertilize the egg. During this time, sperm undergo a plethora of biochemical changes collectively called capacitation (Bailey, 2010; Aitken and Nixon, 2013; Gervasi and Visconti, 2016). The discovery of this phenomenon was crucial to the development of *in vitro* fertilization (Austin, 1951; Chang, 1951, Chang, 1959). Capacitation is characterized by cholesterol efflux, phospholipase activation, and altered membrane fluidity, along with a multitude of biochemical changes (Nolan and Hammerstedt, 1997; Travis and Kopf, 2002; Harrison and Gadella, 2005; Bailey, 2010). Together, these changes render sperm capable of undergoing the acrosome reaction, a unique exocytotic event that is an absolute requirement for sperm to become fusion-competent (Yanagimachi, 1981) (**Figure 1A**).

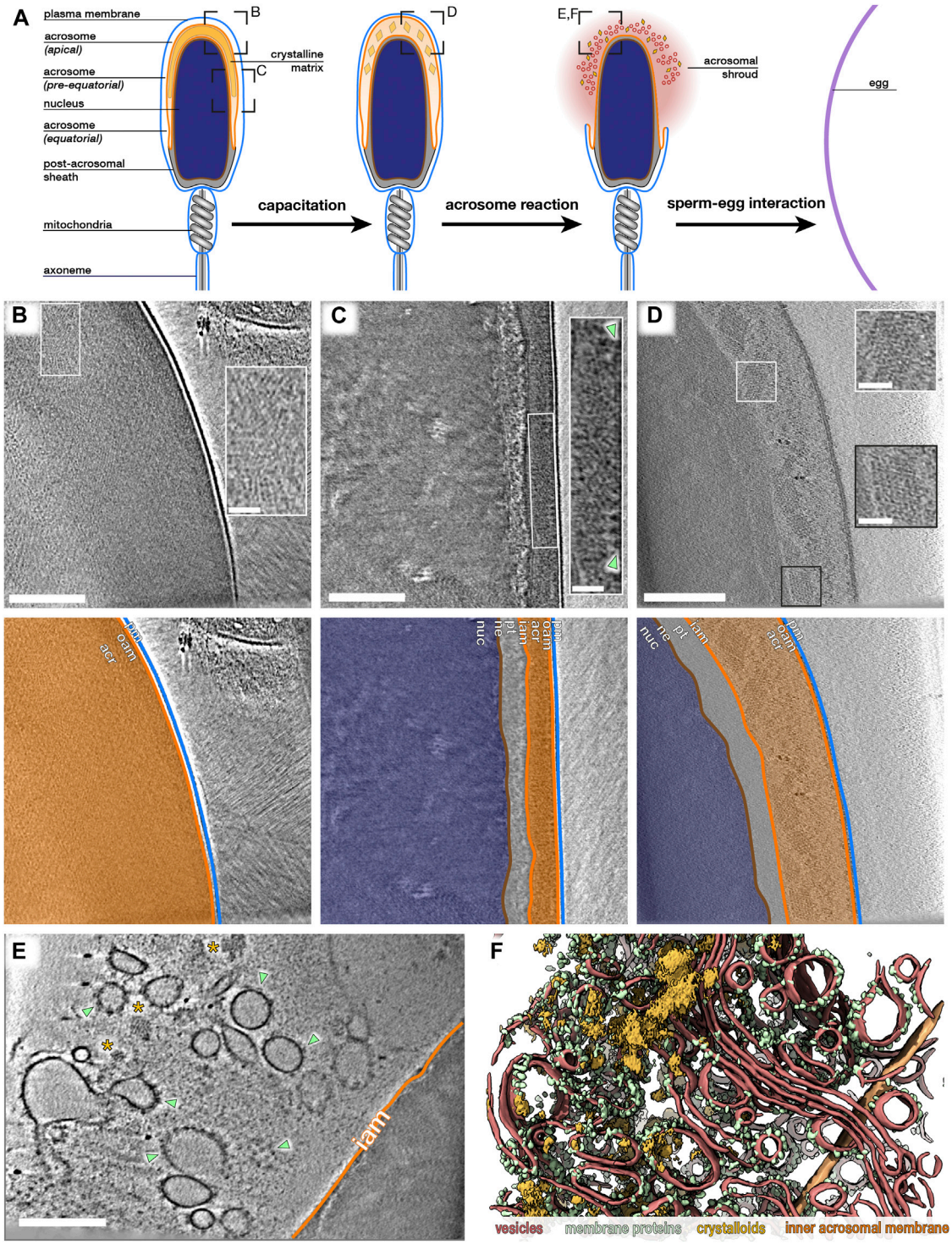

FIGURE 1 | The paracrystalline fraction of the acrosomal matrix progressively disassembles during acrosomal exocytosis. **(A)** Schematic diagram illustrating the morphological changes that mammalian sperm undergo in the female reproductive tract, simulated in this study *in vitro*. Boxed regions indicate approximate locations where data in **(B–F)** were acquired. **(B,C)** Computational slices through Volta phase plate cryo-tomograms of noncapacitated sperm thinned by cryo-focused ion beam milling. Note how the acrosome is dense even in thinned samples. Insets show regions with large paracrystalline patches. Large membrane protein densities are visible on the luminal surface of the outer acrosomal membrane (green arrowheads in inset). **(D)** Computational slice through a defocus-contrast cryotomogram of a sperm cell whose acrosome had swollen after incubation in capacitating media for ~2 h. Note the decondensation of the acrosome and the prominent paracrystalline patches (insets). **(E,F)** Computational slice **(E)** and corresponding three-dimensional reconstruction **(F)** of the acrosomal shroud. The cell was incubated in capacitating media for ~2 h and treated with calcium ionophore for ~30 min. Note the paracrystalline patches (asterisks in **E**, goldenrod in **F**) and membrane protein-decorated vesicles (green arrowheads in **E**, green in **F**). Vesicle membranes are shown in red, and the inner acrosomal membrane is shown in orange. Scale bars: 250 nm; insets: 50 nm Color scheme: orange—outer and inner acrosomal membrane, red—vesiculated plasma and outer acrosomal membranes, green—membrane protein densities, goldenrod—paracrystalline patches.

The acrosome is a large regulated secretory vesicle overlying the anterior two-thirds of the nucleus; its crucial role in mammalian fertilization manifests in the fact that malformation of the acrosome causes infertility in both humans and mice. Three distinct segments of the acrosome can be defined based on their positions along the sperm head (**Figure 1A**): the apical segment extends beyond the nucleus and forms the most anterior region of the acrosome; the principal or pre-equatorial segment forms the major part of the acrosome; and the equatorial segment delimits the posterior part of the acrosome. During acrosomal exocytosis, the plasma membrane fuses with the outer acrosomal membrane at multiple points. This destabilizes the acrosome and liberates its contents, which include several proteins implicated in either penetrating through or binding to the egg vestments (Foster and Gerton, 2016).

Acrosomal exocytosis is not an all-or-nothing event but instead involves the gradual dispersal of vesicle cargo (Hardy et al., 1991; Kim, Foster and Gerton, 2001; Kim and Gerton, 2003). Biochemical analyses defined two classes of acrosome contents: a soluble fraction that is released shortly after the onset of the acrosome reaction, and a matrix fraction that disperses more slowly. Consistent with this, conventional electron microscopy (EM) studies showed discrete zones within the acrosome, including paracrystalline material that extends across large areas of the vesicle in sperm from several mammalian species including the rat (Phillips, 1972), rabbit (Courtens, Courot and Fléchon, 1976; Olson and Winfrey, 1994; Fléchon, 2016), ram, and bull (Courtens, Courot and Fléchon, 1976). However, the structural changes in the acrosomal matrix that mediate differential release of acrosome contents remain undefined.

Another distinctive feature of acrosomal exocytosis is the lack of membrane recycling. The plasma membrane and the outer acrosomal membrane are shed as vesicles, so the sperm head loses a large portion of its limiting membrane while the remainder becomes fusogenic. Acrosome vesiculation has been studied extensively with classical EM (Barros et al., 1967; Russell et al., 1979; Jamil and White, 1981; Nagae et al., 1986; Stock and Fraser, 1987; Yudin et al., 1988; Flaherty and Olson, 1991; Zanetti and Mayorga, 2009; Sosa et al., 2015), identifying acrosome swelling and membrane docking as clear intermediates leading to exocytosis (Zanetti and Mayorga, 2009; Tsai et al., 2010; Sosa et al., 2015). However, the membrane remodeling pathways that ensure the cell remains intact throughout this dramatic vesiculation process remain undefined.

Here, we use cryoelectron tomography (cryo-ET) to image sperm undergoing *in vitro* capacitation and acrosome exocytosis. Cryo-ET provides three-dimensional information about rare events in unfixed, unstained, fully hydrated samples, and thus in close to native conditions (Ng and Gan, 2020). We show that the paracrystalline component of the acrosomal matrix gradually dissolves during acrosomal exocytosis, explaining the differential release previously observed. We also find that the defined ultrastructural organization of the sperm head facilitates a unique fission–fusion mechanism that maintains cell integrity despite drastic membrane vesiculation. We demonstrate that acrosome exocytosis also facilitates massive membrane protein relocalization onto the post-acrosomal plasma membrane, building a platform for interaction with the egg.

RESULTS

In Uncapacitated Sperm, the Plasma Membrane (PM) and the Outer Acrosomal Membrane (OAM) are Closely Apposed Along the Entire Acrosome

We plunge-froze sperm from highly fertile, commercial artificial insemination pigs (*Sus scrofa domestica*) and imaged them using cryo-ET. In intact uncapacitated sperm, the plasma membrane (PM) and the outer acrosomal membrane (OAM) are closely apposed along the entire acrosome (**Figures 1B,C**; **Supplementary Figure S1**). The PM and the OAM are ~8–10 nm apart and lie parallel to each other until the equatorial segment of the acrosome, where the vesicle tapers (**Supplementary Figure S1D–F**). This differs from many classical EM images of uncapacitated sperm, in which the PM and OAM appear wavy with estimated interbilayer distances of >10 nm (Zanetti and Mayorga, 2009; Tsai et al., 2010; Sosa et al., 2015), and demonstrates the benefits of using cryo-ET to visualize acrosomal exocytosis.

The Paracrystalline Fraction of the Acrosomal Matrix Progressively Disassembles During Exocytosis

We sought to determine how the internal organization of the acrosome changes during acrosomal exocytosis. We first imaged acrosome contents in intact uncapacitated sperm cells thinned to ~150–200 nm with cryo-focused ion beam (cryo-FIB) milling (Marko et al., 2006; Rigort et al., 2012). Even after thinning and imaging with the Volta phase plate (VPP) (Danev et al., 2014; Fukuda et al., 2015), the acrosome lumen was still very dense (**Figures 1B,C**). Nonetheless, we observed large patches of paracrystalline material in both the apical and pre-equatorial regions of the acrosome (insets in Figures 1B,C), similar to the structures observed in rat sperm (Phillips, 1972), rabbit sperm (Olson and Winfrey, 1994), and ram sperm (Fléchon, 2016).

To visualize acrosomal exocytosis, we imaged sperm incubated in capacitating media (containing calcium, bicarbonate, and bovine serum albumin) for ~2 h and subsequently treated with calcium ionophore A23187. These protocols are known to induce boar sperm capacitation and acrosome reaction (Tsai et al., 2007; Boerke et al., 2014), which we also confirmed through phosphotyrosine staining and fluorescent lectin staining, respectively (**Supplementary Figure S2**). Following treatment, fully acrosome-reacted sperm could be readily targeted in low-magnification cryo-EM projection images (**Supplementary Figure S3**). These cells were surrounded by a cloud of vesicles (the acrosomal shroud) (**Supplementary Figure S3A**), and their apical regions had become very thin due to the loss of the acrosome (**Supplementary Figure S3B**), allowing us to image them without cryo-FIB milling. We note that acrosomal shrouds

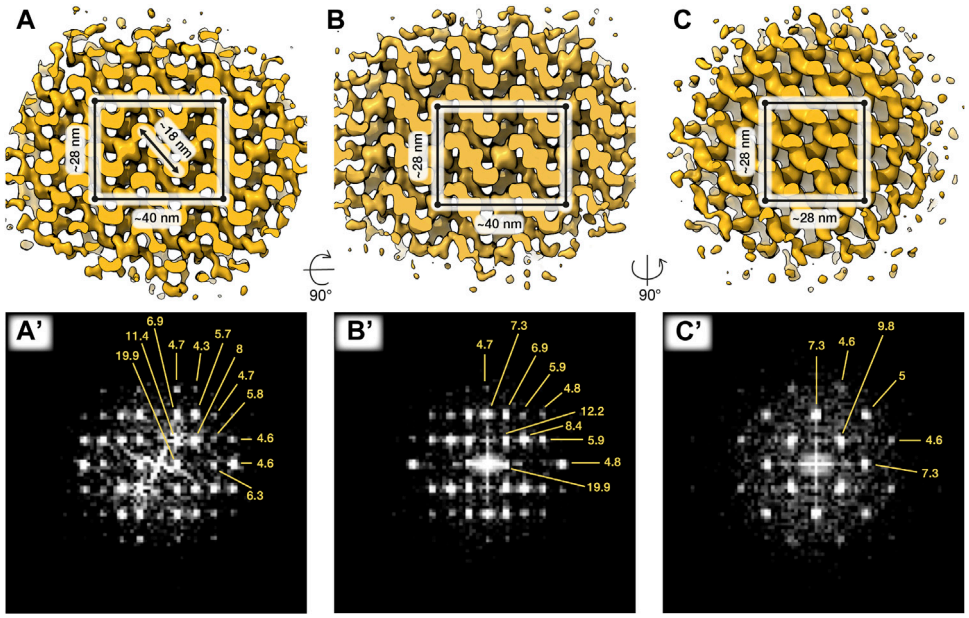

FIGURE 2 | *In situ* structures of paracrystalline patches from capacitated sperm. Three orthogonal isosurface views **(A–C)** and corresponding Fourier transforms **(A'–C')** of a subtomogram average of 87 × 87 × 87 nm paracrystalline patch from swollen acrosomes of boar sperm incubated in capacitating media for ~2 h. The putative tetragonal body-centered unit cell is annotated in **(A–C)**. Averages were generated from ~1,400 particles from 2 cells.

tend to remain associated with sperm heads despite several pipetting and dilution steps before imaging. In our analyses, we excluded sperm in which the plasma membrane peeled off at the equatorial/post-acrosomal regions, which would likely result in loss of cell integrity and thus in cell death (**Supplementary Figures S3C, D**).

We found that the acrosomal shroud consists of a highly heterogeneous population of vesicles that are decorated with membrane proteins (**Figures 1E,F**). Interspersed between these vesicles are the contents of the acrosome, including striking paracrystalline patches that were heterogeneous in size and shape (ionophore: 12/13 tomograms, each from a different cell, from three different animals) (**Figure 1E**; **Supplementary Figure S4**). We also observed paracrystalline patches in acrosomal shrouds of sperm stimulated with progesterone (5/5 tomograms, each from a different cell, from one animal), which has been shown to stimulate the acrosome reaction in human sperm (Harper et al., 2006).

To follow the paracrystalline patches during intermediate stages of exocytosis, we imaged cells incubated in capacitating media without ionophore treatment. Paracrystalline patches were readily visible in swollen acrosomes (**Figure 1D**), where they had already begun to dissociate into smaller fragments. We then used subtomogram averaging to resolve the structure of the paracrystalline patches at a resolution of ~30–40 Å (**Figure 2**). We chose to average from capacitated sperm since the surrounding material was too dense in uncapacitated sperm. The patches were also larger in capacitated sperm than in the shrouds of acrosome-reacted sperm, which facilitated averaging by increasing particle numbers. Our averages reveal that the paracrystalline patches adopt a tetragonal body-centered crystal lattice with apparent unit cell dimensions a = 28 nm, b = 28 nm, and c = 40 nm.

Taken together, our data indicate that the paracrystalline patches in the acrosomal shroud result from disassembly of an initial larger superstructure. The paracrystalline fraction may thus represent the core of the acrosomal matrix, acting as a structural scaffold onto which soluble components of the acrosome are anchored. Their progressive disassembly may represent a mechanism for controlled release of acrosome contents that appears to be conserved across mammals.

An Atypical Membrane Fission-Fusion Pathway Maintains Cell Integrity at the Equatorial Segment

We then sought to trace membrane remodeling intermediates involved in capacitation and acrosomal exocytosis. Sperm within an ejaculate are inherently variable (Buffone, Hirohashi and Gerton, 2014), which precludes a strictly timepoint-based assessment of the reaction coordinate. We instead imaged several cells from several different animals (**Supplementary Table S1**), analyzed the dataset for membrane remodeling intermediates that we could observe consistently, and ordered these stages relative to one another (**Figures 3**, **4**).

We captured a range of intermediates already in capacitated sperm without ionophore stimulation (**Figure 3**), including acrosome swelling, membrane docking, and membrane destabilization (**Supplementary Figure S5**). Acrosome swelling is one of the earliest stages of acrosomal exocytosis (Zanetti and Mayorga, 2009; Sosa et al., 2015) and indeed was observed even in capacitated cells (Boerke et al., 2014). Swelling is associated with decondensation of acrosomal contents, but our tomograms reveal that decondensation is not uniform. Specifically, a dense core

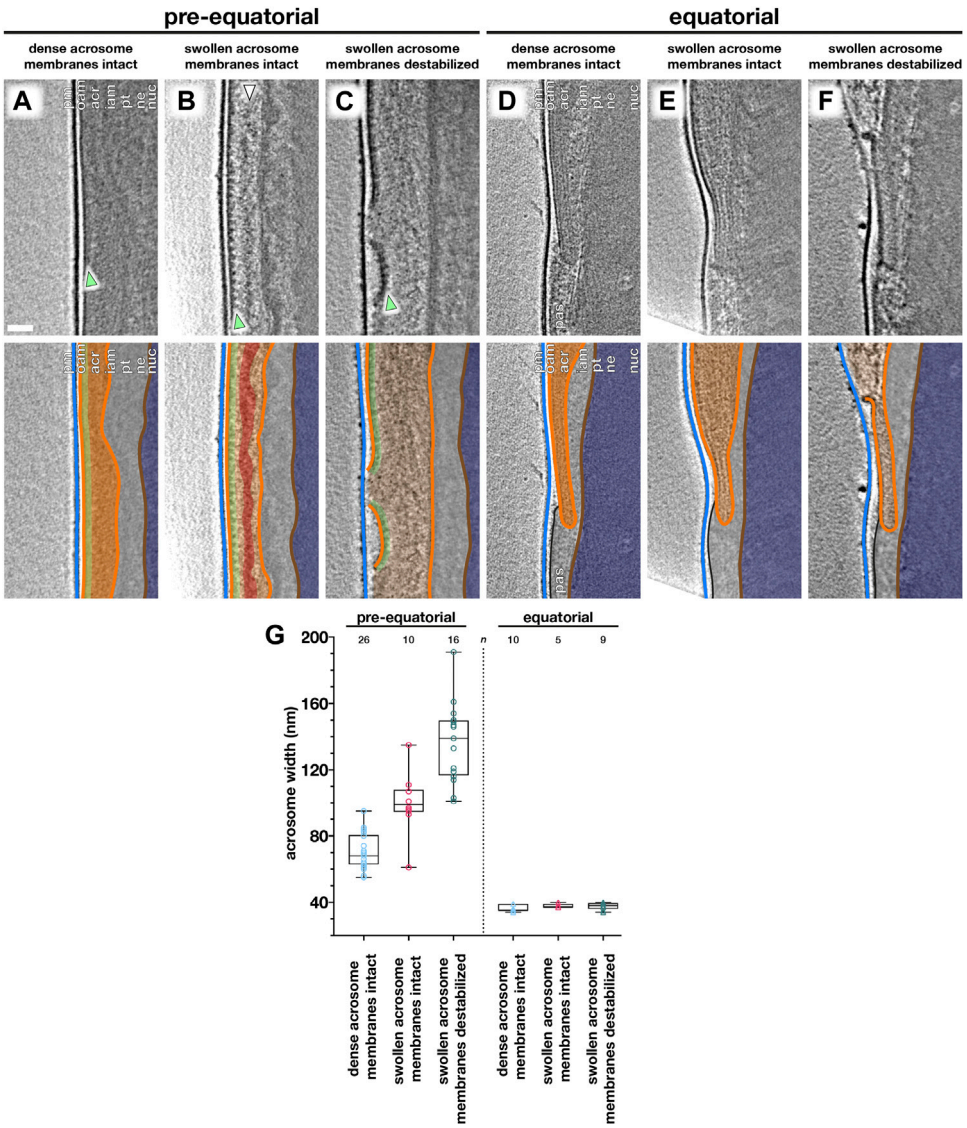

FIGURE 3 | Acrosome swelling is associated with membrane destabilization in capacitated sperm. **(A–F)** Computational slices (top panels) and schematic annotations (bottom panels) of Volta phase plate cryotomograms of the pre-equatorial **(A–C)** and equatorial **(D–F)** region of sperm before **(A,D)** or after (B–C, E–F) a ~2-h incubation in capacitating media without ionophore stimulation. Note the rows of membrane protein densities on the outer acrosomal membrane (green arrowheads in A–C) and the streak of acrosomal matrix that remains condensed during acrosome swelling (white arrowhead in **B**). **(G)** Measurements of acrosomal width at the pre-equatorial (left) and equatorial (right) regions in sperm showing various states of acrosome swelling and membrane destabilization. For each tomogram, acrosome width was measured as the distance between the outer and inner acrosomal membranes at three different locations. Every data point represents the average of these three measurements for the relevant tomogram. Each tomogram is from a different cell (*n* indicates the number of tomograms used for analysis). The boxes indicate the median and interquartile range, while the whiskers indicate the minimum and maximum values. Scale bar: 50 nm. Labels: pm, plasma membrane; oam, outer acrosomal membrane; acr, acrosome; iam, inner acrosomal membrane; pt, perinuclear theca; ne, nuclear envelope; nuc, nucleus; pas, post-acrosomal sheath. Color scheme: blue—plasma membrane, orange—outer and inner acrosomal membranes, green—membrane protein densities, red—condensed acrosomal material, light gray—perinuclear theca and post-acrosomal sheath, brown—nuclear envelope, dark blue—nucleus.

remains near the center of the vesicle (white arrowhead in **Figure 3B**), which is continuous with a thin streak of electron-dense material sandwiched between the OAM and the IAM at the end of the acrosome (white arrowhead in **Figure 4B**). Decondensation also improves contrast in the acrosome, making visible large membrane protein densities on the luminal surface of the OAM (green arrowhead in **Figures 3B,C**). These structures are also visible in VPP tomograms of FIB-milled uncapacitated sperm (green arrowheads in **Figure 1B** inset and **Figure 3A**). The OAM proteins form rows of teeth-like densities, each extending ~14 nm into the OAM lumen and spaced ~18 nm from its neighbors.

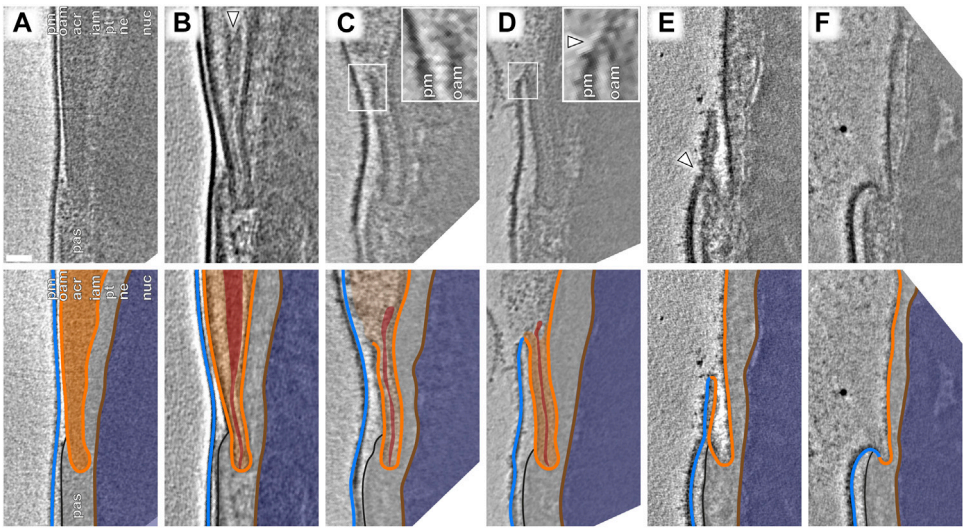

FIGURE 4 | An atypical membrane fission–fusion pathway maintains cell integrity at the equatorial region. **(A–F)** Computational slices (top panels) and corresponding schematic annotations (bottom panels) of Volta phase plate cryotomograms of the equatorial region of sperm incubated for ~2 h in capacitating media without **(A–D)** and with **(E,F)** subsequent ~30-min ionophore stimulation. In **(B)**, the white arrowhead indicates condensed material at the core of the acrosome that is continuous with a thin streak of electron-dense material in the equatorial segment. In **(C)**, the inset shows the point of OAM rupture immediately anterior to the equatorial region. In **(D)**, the inset shows that the OAM has fused (white arrowhead) with the overlying PM at this location. Scale bar: 50 nm. Labels: pm, plasma membrane; oam, outer acrosomal membrane; acr, acrosome; iam. inner acrosomal membrane; pt, perinuclear theca; ne, nuclear envelope; nuc, nucleus; pas, post-acrosomal sheath. Color scheme: blue—plasma membrane, orange—outer and inner acrosomal membranes, red—condensed acrosomal material, light gray—perinuclear theca and post-acrosomal sheath, brown—nuclear envelope, dark blue—nucleus.

We could further distinguish between two stages of acrosome swelling: one in which the acrosome swells but the overlying membranes are still intact (**Figures 3B,E**), and another in which the OAM already destabilizes (**Figures 3C,F**). OAM destabilization is characterized by local membrane rupture (**Figures 3C,F**; **Figure 4C**; **Supplementary Figure S5G–L**). OAM rupture was associated with the extent of acrosome swelling; in cells with ruptured OAMs, the acrosome had swollen to nearly twice its original width (136 ± 24 nm vs. 71 ± 11 nm, with an intermediate value of 100 ± 18 nm in cells with swollen acrosomes but intact membranes) (**Figure 3G**). In contrast, the width of the equatorial segment did not change significantly even in cells with ruptured OAMs (acrosome swollen, membranes destabilized: 38 ± 2 nm; acrosome swollen, membranes intact: 38 ± 1 nm; uncapacitated sperm with dense acrosome, membranes intact: 36 ± 2 nm). Notably, OAM rupture occurred just anterior to the equatorial segment, on average 260 ± 80 nm from the end of the acrosome (mean ± s.d., 8 tomograms, each from a different cell) (**Figure 3F**).

Focusing on the equatorial segment, we observed an atypical membrane fission–fusion pathway that mediates resealing of the sperm head (**Figure 4**). The ruptured end of the OAM fuses with the overlying PM (**Figures 4C,D**; **Supplementary Figure S5J–L**), and after this fusion event, the electron-dense streak also diffuses, leaving a hairpin-shaped membrane (**Figure 4E**, **Supplementary Figure S6A–B**). This hairpin-shaped membrane then constricts and buds off just anterior to the post-acrosomal sheath (**Figure 4E**, arrowhead), yielding the characteristic morphology of acrosome-reacted cells (**Figure 4F**, **Supplementary Figure S6C**).

Acrosomal Exocytosis Transforms the Molecular Landscape of the Sperm Plasma Membrane

After loss of the acrosome, the inner acrosomal membrane (IAM) is the new limiting membrane of the apical segment of the sperm cell (**Figure 1E**). The PM overlying the equatorial/post-acrosomal segment remains intact and is now continuous with the IAM (**Figure 5**). Segmentation of high-contrast tomograms acquired with a VPP revealed that the PM forms a "sheath" around the post-acrosomal region (**Figure 5D**, **Supplementary Figure S6**). Our tomograms also showed tubulovesicular projections overlying the equatorial segment (**Figure 5D**, **Supplementary Figure S6**). These tubular membranes are consistent with those observed by freeze-fracture EM (Aguas and da Silva, 1989). Thus, the acrosome reaction remodels the overall topography of the sperm surface.

We then compared the post-acrosomal segment in uncapacitated versus acrosome-reacted sperm (**Figures 5B,E**; **Supplementary Figure S7**). Inspecting the PM overlying the post-acrosomal sheath reveals major differences in protein decoration. In unreacted cells, the post-acrosomal PM is relatively smooth, with only a few small protein densities protruding from the membrane (**Figure 5B**, **Supplementary Figures S7A–C**) (14/14 tomograms, each from a different cell, from six different animals). In contrast, the post-acrosomal PM was densely packed with membrane protein densities in ~80% of

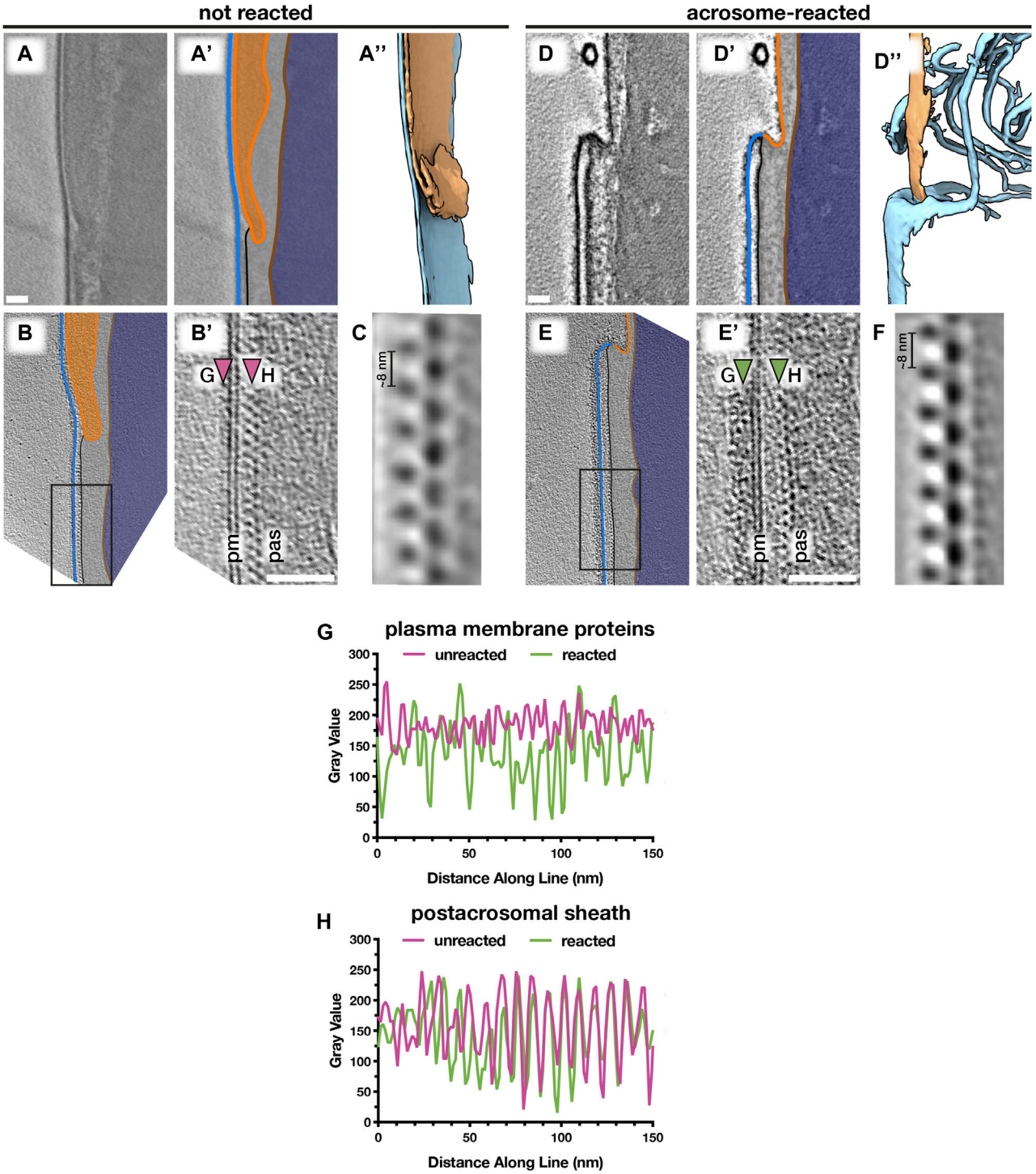

FIGURE 5 | Acrosomal exocytosis transforms the molecular landscape of the sperm plasma membrane. Comparing the post-acrosomal plasma membrane in unreacted **(A–C)** versus acrosome-reacted **(D–F)** reveals major differences in membrane protein decoration. **(A,D)** Computational slices **(A and A',D and D')** and corresponding three-dimensional reconstructions **(A'',D'')** of VPP cryotomograms illustrating how acrosomal exocytosis remodels the topography of the equatorial region. **(B,E)** Computational slices through defocus-contrast cryotomograms illustrating how the post-acrosomal plasma membrane becomes densely packed with membrane proteins after acrosomal exocytosis. **(C,F)** Subtomogram averages of the post-acrosomal sheath from unreacted **(C)** and acrosome-reacted **(F)** cells. **(G,H)** Exemplary linescans illustrating changes in membrane protein density after the acrosome reaction **(G)**, as well as the lack of noticeable change in the post-acrosomal sheath **(H)**. Linescans were taken at the approximate locations marked by arrowheads in **(B') and (E')**. Scale bars: 50 nm. Labels: pm, plasma membrane; pas, post-acrosomal sheath. Color scheme: blue—plasma membrane, orange—outer and inner acrosomal membranes, light gray—perinuclear theca and post-acrosomal sheath, brown—nuclear envelope, dark blue—nucleus.

tomograms of acrosome-reacted cells (30/37 tomograms, each from a different cell, from five different animals) (**Figures 5E,G**; **Supplementary Figures S7D–F**). These densities do not appear to be ordered, which suggests that they represent a range of different conformations, proteins, or protein complexes. Thus, the acrosome reaction results in massive membrane protein relocalization that alters the molecular landscape of the sperm surface.

We then used subtomogram averaging to define the substructure of the post-acrosomal sheath in more detail (**Figures 5C,F**). The peripheral layer of the post-acrosomal sheath, immediately underlying the PM, consists of a multilayered structure with an ~8-nm repeating unit. Our averages reveal that neither the substructure nor the overall organization of the post-acrosomal sheath changes noticeably after acrosomal exocytosis, which is consistent with measurements directly from tomograms (**Figure 5H**). Similarly, the distance between the PM and the post-acrosomal sheath remains relatively unchanged (unreacted: 15 ± 2 nm, reacted: 18 ± 3 nm).

DISCUSSION

Gradual Disassembly of the Paracrystalline Matrix may Represent a Mechanism for Controlled Release of Acrosome Contents

Leading up to and during acrosomal exocytosis, acrosome contents disperse at rates dependent on their partitioning into either soluble or particulate fractions. The particulate fraction, also known as the acrosomal matrix, disperses gradually in a process dependent on alkalization and proteolytic self-digestion (Buffone et al., 2008). However, we do not understand the underlying structural transitions in the acrosomal matrix that regulate the dispersal of acrosomal contents. Studies of acrosomal matrix dispersal are often performed on guinea pig sperm, which have large acrosomes partitioned into subdomains easily visible by transmission EM (Flaherty and Olson, 1988; Hardy et al., 1991; Olson and Winfrey, 1994; Kim, Foster and Gerton, 2001). Here, we use cryo-ET to show that the acrosome is structurally compartmentalized also in boar sperm (**Figure 1**), which have comparatively thin acrosomes and no obvious subdomains when viewed by conventional EM (Buffone et al., 2008).

Specifically, we find an extensive Paracrystalline fraction in the boar sperm acrosome. Although Paracrystalline structures have been demonstrated previously in acrosomes of other mammals, they were not followed throughout capacitation and acrosomal exocytosis. Our data now show that the Paracrystalline fraction begins to disassemble during capacitation (**Figure 1D**) and continues to do so during acrosomal exocytosis, resulting in small patches scattered among the vesicles of the acrosomal shroud (**Figures 1E,F**). Gradual disassembly of the Paracrystalline matrix thus represents a plausible mechanism for controlled release of acrosome contents. Refining this model will require further studies aimed at determining the nature of the Paracrystalline fraction—for instance, whether it represents a scaffolding structure or a storage phase for inactive enzymes. The subtomogram averages we present here (**Figure 2**) can help toward this goal by providing constraints on the molecular dimensions of candidate proteins.

Cryo-ET Reveals how Capacitation-Associated Membrane Destabilization Relates to the Membrane Fission–Fusion Processes Involved in Acrosomal Exocytosis

Our observations suggest that acrosome swelling relates directly to membrane destabilization (**Figure 3**), which is likely caused by an increase in membrane tension in addition to known changes in membrane composition mediated by cholesterol efflux and phospholipase activation (Aitken and Nixon, 2013; Asano, Nelson-Harrington and Travis, 2013). A role for swelling-dependent membrane destabilization is also supported by observations that hyper-osmotic conditions inhibit the acrosome reaction (Bielfeld, Jeyendran and Zaneveld, 1993) and that lysophosphatidylcholine, a positive curvature amphiphile that reduces the energetic barrier for membrane rupture (Glushakova et al., 2005), promotes the reaction (Parrish et al., 1988; de Lamirande, Leclerc and Gagnon, 1997). Meanwhile, the equatorial region is stabilized by the electron-dense core of the acrosome (**Figures 3D–F**) and the post-acrosomal region likewise stabilized by the post-acrosomal sheath. Thus, the precise organization of the sperm head facilitates the rupture–fusion pathway that maintains cell integrity despite destabilization and vesiculation of the rest of the acrosome (**Figure 4**).

The intermediates we observe do not appear to fit the canonical fusion-by-hemifusion pathway; instead, the presence of membrane edges is reminiscent of the rupture–insertion pathway (Chlanda et al., 2016; Haldar et al., 2019). Whether fusion proceeds via hemifusion or via rupture–insertion depends on membrane spontaneous curvature and hence on lipid composition, with the rupture–insertion pathway strongly favoring cholesterol-poor bilayers (Chlanda et al., 2016; Haldar et al., 2019). This may be particularly relevant given that one of the molecular signatures of capacitation is cholesterol efflux.

Acrosomal exocytosis transforms the molecular landscape of the sperm plasma membrane

Acrosomal exocytosis is an absolute requirement for mammalian sperm to fuse with the egg (Yanagimachi, 1981). Fluorescence microscopy has shown that as a result of the acrosome reaction, Izumo1 relocalizes onto the plasma membrane, allowing it to interact with its oocyte-borne partner, Juno, to mediate sperm-egg adhesion (Satouh et al., 2012). However, the Izumo1–Juno interaction is not sufficient to mediate membrane fusion (Bianchi et al., 2014). Our understanding of sperm–egg fusion is hampered by the fact that, beyond the translocation of Izumo1, we know very little about what happens to the molecular landscape of the sperm surface after the acrosome reaction.

Here, we show that acrosomal exocytosis transforms both the micron-scale topography and the molecular landscape of the

sperm surface (**Figure 5**). We find that the post-acrosomal plasma membrane becomes heavily decorated with membrane protein densities. Such changes may be due to the relocalization of membrane proteins, similar to the phenomenon observed by freeze-fracture EM for the acrosomal cap region (Aguas and da Silva, 1989), or to the binding of liberated acrosomal proteins to pre-existing receptors. The post-acrosomal membrane protein densities do not appear to be ordered, which suggests that they represent a range of different conformations, proteins, or protein complexes. Indeed, in addition to Izumo1, there are now a number of proteins on mammalian sperm that are known to be essential for sperm–egg binding and fusion (Inoue et al., 2005; Fujihara et al., 2020; Lamas-Toranzo et al., 2020; Noda et al., 2020). Our results therefore complement the emerging view that mammalian sperm–egg fusion involves several molecular species acting in concert. Our study also opens avenues for future work into how these various players are organized on the sperm membrane at the nanoscale.

MATERIALS AND METHODS

Sperm Washing, Capacitation, and Acrosome Reaction

Freshly ejaculated pig (*Sus scrofa domestica*) semen was purchased from an artificial insemination company (AIM Varkens KI, Veghel, Nederland). Semen was typically diluted in Beltsville thawing solution (BTS: 205 mM glucose, 20.4 mM NaCl, 5.4 mM KCl, 15 mM $NaHCO_3$, 3.4 mM EDTA) and stored at 18°C until use. Sperm were used within 1 day of delivery. Sperm were gently layered onto a discontinuous gradient consisting of 2 ml 70% Percoll overlaid with 4 ml of 35% Percoll (GE Healthcare), both in 1X HEPES-buffered saline (HBS: 20 mM HEPES, 137 mM NaCl, 10 mM glucose, 2.5 mM KCl, 1% kanamycin, pH 7.6). Pelleted cells were washed once in 1X DPBS (Sigma), resuspended in 1 ml of 1X DPBS, and counted.

Capacitation and acrosome reaction protocols were based on methods previously validated for pig sperm (Tsai et al., 2007). Washed sperm were resuspended in 1X TALP (20 mM HEPES, 90 mM NaCl, 21.7 mM sodium lactate, 5 mM glucose, 3.1 mM KCl, 1 mM sodium pyruvate, 0.4 mM $MgSO_4$, 0.3 mM NaH_2PO_4, 2 mM $CaCl_2$, 15 mM $NaHCO_3$, 100 μg/ml kanamycin, 0.3% w/v fatty acid-free BSA (Sigma), pH 7.4) at concentrations in the range of 10–20 × 10^6 cells/ml. Sperm were allowed to capacitate for between 2 and 2.5 h at 37°C, 5% CO_2. In order to stimulate the acrosome reaction more rapidly and in a larger percentage of cells, calcium ionophore A23187 (Sigma) was added to capacitated cells to a final concentration of 5 or 3 μM. Cells were incubated for either a further 30 min (for ionophore) at 37°C, 5% CO_2. As a supplementary experiment to verify the presence of paracrystalline patches using another AR inducer, we also imaged cells stimulated with progesterone (Sigma) at a final concentration of 3 μM.

For flow cytometry, cells were first washed with 1X DPBS and their concentration adjusted to 30–50 × 10^6 cells/ml. Sperm were then stained with propidium iodide (LifeTechnologies) and with PNA-FITC (Sigma), both at a final concentration of 1 μg/ml. Sperm were then diluted 1/100 to 0.3–0.5 × 10^6 cells/ml and analyzed using a BD FACSCanto II flow cytometer. Viable, acrosome-reacted cells were defined as those in the PI^-FITC^+ quadrant of the cytogram.

To assess capacitation, cells were stained with antibodies against phosphorylated tyrosine. Either uncapacitated or capacitated sperm cells were allowed to settle in 8-well ibidi μ-slides for 15 min, after which paraformaldehyde was added to a final concentration of 4%. After 30 min of fixation, cells were washed with PBS and subsequently permeabilized with 0.5% Triton X-100 in PBS for 15 min. Cells were then washed with PBS three times, then blocked overnight at 4°C with 1% BSA in PBS with 0.05% Tween 20 (PBS-T). After blocking, cells were incubated with primary antibody (anti-phosphotyrosine clone 4G10 diluted 1:200 in PBS-T + 1% BSA) for 2 h at room temperature (RT). Cells were washed in PBS three times and incubated with secondary antibody (goat antimouse AlexaFluor-488 diluted 1:100 in PBS-T + 1% BSA) for 1 h at RT. Cells were again washed with PBS three times, and nuclei were counterstained with Hoechst 33342 for 30 min in PBS. After three final PBS washes, FluorSave mounting medium was added to the wells. Slides were imaged using a CorrSight microscope (ThermoFisher) operating in the spinning disk mode.

Cryo-EM Grid Preparation

Typically, 3 μl of a suspension containing either 1–3x10^6 cells/ml (for whole cell tomography) or 20–30 × 10^6 cells/ml (for cryo-FIB milling) was pipetted onto either glow-discharged Quantifoil R 2/1 200-mesh holey carbon or Quantifoil 200-mesh lacey carbon grids. One microliter of a suspension of BSA-conjugated gold beads (Aurion) was added, and the grids then blotted manually from the back (opposite the side of cell deposition) for ~3 s (for whole cell tomography) or ~5–6 s (for cryo-FIB milling) using a manual plunge-freezer (MPI Martinsried). Grids were immediately plunged into either liquid ethane or a liquid ethane–propane mix (37% ethane) (Tivol et al., 2008), cooled to liquid nitrogen temperature. Grids were stored under liquid N_2 until imaging.

Cryo-Focused Ion Beam Milling

Grids were mounted into modified Autogrids (FEI) for mechanical support. Clipped grids were loaded into an Aquilos (FEI) dual-beam cryo-focused ion beam/scanning electron microscope (cryo-FIB/SEM). All SEM imaging was performed at 2 kV and 13 pA, whereas FIB imaging for targeting was performed at 30 kV and 10 pA. Milling was typically performed with a stage tilt of 18°, so lamellae were inclined 11° relative to the grid. Each lamella was milled in four steps: an initial rough mill at 1 nA beam current, an intermediate mill at 300 pA, a fine mill at 100 pA, and a polishing step at 30 pA. Lamellae were milled with the wedge pre-milling method described in Schaffer et al. (2017) and with stabilizing expansion segments described in Wolff et al. (2019).

Tilt Series Acquisition

Tilt series was acquired on either a Talos Arctica (FEI) operating at 200 kV or a Titan Krios (FEI) operating at 300 kV, both

equipped with a postcolumn energy filter (Gatan) in zero-loss imaging mode with a 20-eV energy-selecting slit. All images were recorded on a K2 Summit direct electron detector (Gatan) in either counting or super-resolution mode with dose fractionation. Tilt series was collected using SerialEM (Mastronarde, 2005) at a target defocus of between −4 and −6 μm (conventional defocus-contrast) or between −0.5 and −1.5 μm (for tilt series acquired with the Volta phase plate). Tilt series were typically recorded using either strict or grouped dose-symmetric schemes either spanning ±56° in 2° increments or ±54° in 3° increments, with total dose limited to ~100 $e^{-}/Å^2$.

Tomogram Reconstruction

Frames were aligned either post-acquisition using Motioncor2 1.2.1 (Zheng et al., 2017) or on-the-fly using Warp (Tegunov and Cramer, 2019). Frames were usually collected in counting mode; when super-resolution frames were used, they were binned 2X during motion correction. Tomograms were reconstructed in IMOD (Kremer et al., 1996) using weighted back-projection, with a SIRT-like filter (Zeng, 2012) applied for visualization and segmentation. Defocus-contrast tomograms were CTF-corrected in IMOD using *ctfphaseflip,* while VPP tomograms were left uncorrected.

Tomogram Segmentation

Tomogram segmentation was generally performed semiautomatically. Initial segmentation was performed using the neural network-based TomoSeg package in EMAN 2.21. Segmentation was then refined manually in either Avizo 9.2.0 (FEI) or Chimera 1.12. Membrane distance measurements were performed using built-in functions in Avizo 9.2.0.

Subtomogram Averaging of Paracrystalline Patches

Subtomogram averaging with missing wedge compensation was performed using PEET 1.13.0 (Nicastro et al., 2006; Heumann et al., 2011). Alignments were performed first on 4x-binned data, after which aligned positions and orientations were transferred to 2x-binned data using scripts shared by Dr. Daven Vasishtan.

Particle positions were seeded by generating a three-dimensional grid of points in paracrystalline patches using the *gridInit* program. All particle orientations were randomized and initial alignments allowed for full rotational searches around all axes. To ensure consistency, two independent initial alignments were performed, each using a randomly selected particle from a separate tomogram as an initial reference. Since alignments converged on a similar structure, alignments were continued. The dataset was cleaned by 1) removing all particles with a cross-correlation value less than one standard deviation above the mean (which removed poorly aligning particles such as those at the edges of paracrystalline patches) and by 2) removing overlapping particles. The orientations of the remaining particles were again randomized and another alignment performed. After a final particle cleanup by classification, a final restricted alignment run was performed. Averages presented in the manuscript were filtered to the estimated resolution based on the Fourier shell correlation (FSC) at a cutoff of 0.5 (Nicastro et al., 2006).

Measurements and Quantification

All measurements were performed on ~20-nm-thick central tomographic slices. Acrosomal width was measured manually in IMOD as the distance between the outer and inner acrosomal membranes. For each tomogram, three measurements were recorded at different locations to account for slight variations in the shape of the acrosome. Linescans for measurement of the post-acrosomal sheath were performed in Fiji v 2.0.0-rc-69/1.52p.

SIGNIFICANCE

Mammalian sperm must undergo a complex series of biochemical and morphological changes in the female reproductive tract in order to become fertilization-competent. These changes culminate in acrosomal exocytosis, during which multiple membrane fusions destabilize the acrosomal vesicle and liberate its contents, which include proteins implicated in penetrating and binding to the egg vestments. Here, we use cryoelectron tomography to visualize acrosomal exocytosis intermediates in unfixed, unstained sperm. Our results suggest structural bases for how gradual dispersal of acrosome contents is regulated, as well as for how the cell remains intact after losing much of its plasma membrane. We also show that acrosomal exocytosis transforms both the micron-scale topography and the nanoscale molecular landscape of the sperm surface, thus priming it for interaction and fusion with the egg. These findings yield important insights into sperm physiology and contribute to our understanding of the fundamental yet enigmatic process of mammalian fertilization.

DATA AVAILABILITY STATEMENT

The original contributions presented in the study are included in the article/**Supplementary Material**, further inquiries can be directed to the corresponding author. Subtomogram averages of paracrystalline patches from capacitated boar sperm have been deposited to the Electron Microscopy Data Bank (EMDB) with deposition number: EMD-13877.

AUTHOR CONTRIBUTIONS

ML and RR prepared samples for cryo-EM. ML, RR, and TZ-B-M collected and analyzed cryo-ET data. ML, RR, BG, and TZ-B-M wrote the manuscript.

FUNDING

This work was funded by NWO Start-Up Grant 740.018.007 to TZ-B-M, and ML is supported by a Clarendon Fund-Nuffield Department of Medicine Prize Studentship.

ACKNOWLEDGMENTS

The authors thank Dr. M Vanevic for excellent computational support, and Dr. SC Howes, Ingr. CTWM Schneijdenberg and JD Meeldijk for managing and maintaining the Utrecht University EM Square facility. The authors also thank S Leemans and L Teeuwen for their help with sperm preparation in initial stages of the project. This work benefitted from access to the Netherlands Center for Electron Nanoscopy (NeCEN) with support from operators Dr. RS Dillard and Dr. CA Diebolder and IT support from B Alewijnse.

SUPPLEMENTARY MATERIAL

The Supplementary Material for this article can be found online at: https://www.frontiersin.org/articles/10.3389/fcell.2021.765673/full#supplementary-material

Supplementary Figure S1 | The plasma membrane and the outer acrosomal membrane are closely spaced even in noncapacitated sperm. **(A–C)** Low-magnification high-dose cryo-EM projection images of noncapacitated boar sperm heads. Digital zooms show close apposition between the plasma membrane and the outer acrosomal membrane at the apical **(i)**, pre-equatorial **(ii)**, and equatorial **(iii)** regions. **(D–F)** Left panels show three-dimensional reconstructions of the plasma membrane and the outer acrosomal membrane at the apical **(D)**, pre-equatorial **(E)**, and equatorial **(f)** regions. The plasma membrane is colored based on distance from the outer acrosomal membrane, which is shown as a cutaway view in orange. Right panels show corresponding histograms of intermembrane distances. Scale bars: **(A–C)** 1 μm; digital zooms: 250 nm Labels: pm, plasma membrane; oam, outer acrosomal membrane; pas, post-acrosomal sheath.

Supplementary Figure S2 | Flow-cytometric assessment of acrosome reaction efficiency. **(A,B)** Flow cytograms of noncapacitated sperm **(A)** and sperm stimulated to acrosome react with ionophore A23187 **(B)**. **(C)** Proportion of viable acrosome-reacted sperm (PI^-, $PNA\text{-}FITC^+$) as assessed by flow cytometry. Bar graphs show mean ± standard deviation and summarize three independent experiments on three separate animals. **(D)** Fluorescence microscopy-based assessment of the tyrosine phosphorylation response in capacitated pig sperm.

Supplementary Figure S3 | Distinguishing acrosome-reacted sperm from membrane-disrupted sperm in low-magnification cryo-EM projection images. Low-magnification high-dose cryo-EM projection images of acrosome-reacted **(A,B)** and membrane-disrupted **(C,D)** sperm. Note how acrosome-reacted sperm successfully re-seal at the equatorial/post-acrosomal region (**A–B**, white arrows in digital zooms); in contrast, membrane-disrupted sperm have also lost the plasma membrane overlying the post-acrosomal sheath (**C–D**, black arrows in digital zooms). Also note how the apical region becomes very thin in acrosome-reacted cells; in contrast, membrane-disrupted sperm retain an acrosomal ghost around their heads. Scale bars: (**A–D)** 1 μm; digital zooms: 250 nm Labels: pm, plasma membrane; oam, outer acrosomal membrane; iam, inner acrosomal membrane; pas, post-acrosomal sheath; nuc, nucleus; shroud, acrosomal shroud Color scheme: blue—plasma membrane, orange—inner acrosomal membrane, black—post-acrosomal sheath, red—acrosomal shroud.

Supplementary Figure S4 | Additional examples of paracrystalline patches in the acrosomal shroud of acrosome-reacted cells. Computational slices through Volta phase plate cryotomograms of the acrosomal shroud collected at the apical region of sperm stimulated to undergo acrosomal exocytosis with either calcium ionophore **(A,B)** or progesterone **(C,D)**. The boundary of the cell, which is now delimited by the inner acrosomal membrane (iam), is traced in orange. Note the presence of paracrystalline patches (asterisks) of varying shapes and sizes in all tomograms. Scale bars: 250 nm Labels: iam, inner acrosomal membrane; nuc, nucleus.

Supplementary Figure S5 | Additional examples of membrane remodeling intermediates observed in sperm incubated in capacitating media without ionophore stimulation. Computational slices through cryotomograms of sperm with **(A–C)** swollen acrosomes and intact membranes; **(D–F)** swollen acrosomes and locally docked membranes (insets); and **(G–L)** profusely swollen acrosomes and destabilized membranes at the pre-equatorial **(G–I)** and equatorial regions **(J–L)**. Tomograms in **(A,B,D,I,J, and L)** were acquired with the Volta phase plate, while tomograms in **(C,E,F,G,H, and K)** were acquired with defocus-contrast. Scale bars: 100 nm Labels: pm, plasma membrane; oam, outer acrosomal membrane; iam, inner acrosomal membrane; pt, perinuclear theca; pas, post-acrosomal sheath; nuc, nucleus Color scheme: blue—plasma membrane, orange—outer and inner acrosomal membranes, green—membrane protein densities, gray—perinuclear theca and post-acrosomal sheath, brown—nuclear envelope, dark blue—nucleus.

Supplementary Figure S6 | Additional examples of the remodeled topography of acrosome-reacted cells. **(A–C)** Computational slices and **(A'–C')** corresponding three-dimensional reconstructions of Volta phase plate cryotomograms of acrosome-reacted sperm. Scale bar: 250 nm Labels: pm, plasma membrane; iam, inner acrosomal membrane; pas, post-acrosomal sheath; ne, nuclear envelope; nuc, nucleus Color scheme: blue—plasma membrane, orange—inner acrosomal membrane, black—post-acrosomal sheath, brown—nuclear envelope.

Supplementary Figure S7 | Additional examples of membrane protein relocalization onto the post-acrosomal plasma membrane of acrosome reacted cells. Computational slices through cryotomograms of the equatorial/post-acrosomal region in uncapacitated, noncapacitated **(A–C)**, and acrosome-reacted **(D–F)** sperm. The change in membrane protein decoration (arrowheads in **D–F**) is seen consistently even in three different imaging conditions: intermediate-magnification defocus contrast **(A,D)**, high-magnification defocus contrast **(B,E)**, and high-magnification Volta phase plate contrast **(C,F)**. Scale bars: 100 nm Labels: pm, plasma membrane; acr, acrosome; pas, post-acrosomal sheath; ne, nuclear envelope; nuc, nucleus Color scheme: blue—plasma membrane, orange—outer and inner acrosomal membranes, gray—perinuclear theca and post-acrosomal sheath, brown—nuclear envelope, dark blue—nucleus.

Supplementary Table S1 | Dataset summary reporting number of tomograms in the dataset representing each membrane remodeling intermediate.

REFERENCES

Aguas, A. P., and da Silva, P. P. (1989). Bimodal Redistribution of Surface Transmembrane Glycoproteins during Ca2+-dependent Secretion (Acrosome Reaction) in Boar Spermatozoa. *J. Cell Sci* 93 (Pt 3), 467–479. doi:10.1242/jcs.93.3.467

Aitken, R. J., and Nixon, B. (2013). Sperm Capacitation: A Distant Landscape Glimpsed but Unexplored. *Mol. Hum. Reprod.* 19 (12), 785–793. doi:10.1093/molehr/gat067

A.P. Harrison, R., and Gadella, B. M. (2005). Bicarbonate-induced Membrane Processing in Sperm Capacitation. *Theriogenology* 63 (2), 342–351. doi:10.1016/j.theriogenology.2004.09.016

Asano, A., Nelson-Harrington, J. L., and Travis, A. J. (2013). Phospholipase B Is Activated in Response to Sterol Removal and Stimulates Acrosome Exocytosis in Murine Sperm. *J. Biol. Chem.* 288 (39), 28104–28115. doi:10.1074/jbc.M113.450981

Austin, C. (1951). Observations on the Penetration of the Sperm into the Mammalian Egg. *Aust. Jnl. Bio. Sci.* 4 (4), 581. doi:10.1071/BI9510581

Bailey, J. L. (2010). Factors Regulating Sperm Capacitation. *Syst. Biol. Reprod. Med.* 56 (5), 334–348. doi:10.3109/19396368.2010.512377

Barros, C., Bedford, J. M., Franklin, L. E., and Austin, C. R. (1967). Membrane Vesiculation as a Feature of the Mammalian Acrosome reactionThe Journal of Cell Biology. *Rockefeller Univ. Press* 34 (3), C1–C5. doi:10.1083/jcb.34.3.C1

Bianchi, E., Doe, B., Goulding, D., and Wright, G. J. (2014). Juno Is the Egg Izumo Receptor and Is Essential for Mammalian Fertilization. *Nature* 508 (7497), 483–487. doi:10.1038/nature13203

Bielfeld, P., Jeyendran, R. S., and Zaneveld, L. J. D. (1993). Andrology: Osmo-Sensitivity of the Human Sperm Acrosome Reaction. *Hum. Reprod.* 8 (8), 1235–1239. doi:10.1093/oxfordjournals.humrep.a138233

Boerke, A., van der Lit, J., Lolicato, F., Stout, T. A. E., Helms, J. B., and Gadella, B. M. (2014). Removal of GPI-Anchored Membrane Proteins Causes Clustering of Lipid Microdomains in the Apical Head Area of Porcine Sperm. *Theriogenology* 81 (4), 613–624. doi:10.1016/j.theriogenology.2013.11.014

Buffone, M. G., Foster, J. A., and Gerton, G. L. (2008). The Role of the Acrosomal Matrix in Fertilization. *Int. J. Dev. Biol.* 52 (5–6), 511–522. doi:10.1387/ijdb.072532mb

Buffone, M. G., Hirohashi, N., and Gerton, G. L. (2014). Unresolved Questions Concerning Mammalian Sperm Acrosomal Exocytosis1. *Biol. Reprod.* 90 (5), 1–8. doi:10.1095/biolreprod.114.117911

Chang, M. C. (1959). Fertilization of Rabbit Ova *In Vitro*. *Nature* 184 (4684), 466–467. doi:10.1038/184466a0

Chang, M. C. (1951). Fertilizing Capacity of Spermatozoa Deposited into the Fallopian Tubes. *Nature* 168 (4277), 697–698. doi:10.1038/168697b0

Chlanda, P., Mekhedov, E., Waters, H., Schwartz, C. L., Fischer, E. R., Ryham, R. J., et al. (2016). The Hemifusion Structure Induced by Influenza Virus Haemagglutinin Is Determined by Physical Properties of the Target Membranes. *Nat. Microbiol.* 1 (6), 16050. doi:10.1038/nmicrobiol.2016.50

Courtens, J. L., Courot, M., and Fléchon, J. E. (1976). The Perinuclear Substance of Boar, Bull, Ram and Rabbit Spermatozoa. *J. Ultrastruct. Res.* 57 (1), 54–64. doi:10.1016/S0022-5320(76)80054-8

Danev, R., Buijsse, B., Khoshouei, M., Plitzko, J. M., and Baumeister, W. (2014). Volta Potential Phase Plate for In-Focus Phase Contrast Transmission Electron Microscopy. *Proc. Natl. Acad. Sci.* 111 (44), 15635–15640. doi:10.1073/pnas.1418377111

de Lamirande, E., Leclerc, P., and Gagnon, C. (1997). Capacitation as a Regulatory Event that Primes Spermatozoa for the Acrosome Reaction and Fertilization. *Mol. Hum. Reprod.* 3 (3), 175–194. doi:10.1093/molehr/3.3.175

Flaherty, S. P., and Olson, G. E. (1988). Membrane Domains in guinea Pig Sperm and Their Role in the Membrane Fusion Events of the Acrosome Reaction. *Anat. Rec.* 220 (3), 267–280. doi:10.1002/ar.1092200307

Flaherty, S. P., and Olson, G. E. (1991). Ultrastructural Analysis of the Acrosome Reaction in a Population of Single guinea Pig Sperm. *Anat. Rec.* 229 (2), 186–194. doi:10.1002/ar.1092290205

Fléchon, J.-E. (2016). The Acrosome of Eutherian Mammals. *Cell Tissue Res* 363 (1), 147–157. doi:10.1007/s00441-015-2238-0

Foster, J. A., and Gerton, G. L. (2016). "The Acrosomal Matrix," in *Advances in Anatomy, Embryology, and Cell Biology*, 15–33. doi:10.1007/978-3-319-30567-7_2

Fujihara, Y., Lu, Y., Noda, T., Oji, A., Larasati, T., Kojima-Kita, K., et al. (2020). Spermatozoa Lacking Fertilization Influencing Membrane Protein (FIMP) Fail to Fuse with Oocytes in Mice. *Proc. Natl. Acad. Sci. USA* 117 (17), 9393–9400. doi:10.1073/pnas.1917060117

Fukuda, Y., Laugks, U., Lučić, V., Baumeister, W., and Danev, R. (2015). Electron Cryotomography of Vitrified Cells with a Volta Phase Plate. *J. Struct. Biol.* 190 (2), 143–154. doi:10.1016/j.jsb.2015.03.004

Gervasi, M. G., and Visconti, P. E. (2016). Chang's Meaning of Capacitation: A Molecular Perspective. *Mol. Reprod. Dev.* 83 (10), 860–874. doi:10.1002/mrd.22663

Glushakova, S., Yin, D., Li, T., and Zimmerberg, J. (2005). Membrane Transformation during Malaria Parasite Release from Human Red Blood Cells. *Curr. Biol.* 15 (18), 1645–1650. doi:10.1016/j.cub.2005.07.067

Haldar, S., Mekhedov, E., McCormick, C. D., Blank, P. S., and Zimmerberg, J. (2019). Lipid-dependence of Target Membrane Stability during Influenza Viral Fusion. *J. Cell Sci.* 132 (4), jcs218321. doi:10.1242/jcs.218321

Hardy, D. M., Oda, M. N., Friend, D. S., and Huang, T. T. F. (1991). A Mechanism for Differential Release of Acrosomal Enzymes during the Acrosome Reaction. *Biochem. J.* 275 (3), 759–766. doi:10.1042/bj2750759

Harper, C. V., Barratt, C. L. R., Publicover, S. J., and Kirkman-Brown, J. C. (2006). Kinetics of the Progesterone-Induced Acrosome Reaction and its Relation to Intracellular Calcium Responses in Individual Human Spermatozoa1. *Biol. Reprod.* 75 (6), 933–939. doi:10.1095/biolreprod.106.054627

Heumann, J. M., Hoenger, A., and Mastronarde, D. N. (2011). Clustering and Variance Maps for Cryo-Electron Tomography Using Wedge-Masked Differences. *J. Struct. Biol.* 175 (3), 288–299. doi:10.1016/j.jsb.2011.05.011

Inoue, N., Ikawa, M., Isotani, A., and Okabe, M. (2005). The Immunoglobulin Superfamily Protein Izumo Is Required for Sperm to Fuse with Eggs. *Nature* 434 (7030), 234–238. doi:10.1038/nature03362

Jamil, K., and White, I. G. (1981). Induction of Acrosomal Reaction in Sperm with Lonophore A23187 and Calcium. *Arch. Androl.* 7, 283–292. doi:10.3109/01485018108999319

Kim, K.-S., Foster, J. A., and Gerton, G. L. (2001). Differential Release of Guinea Pig Sperm Acrosomal Components during Exocytosis1. *Biol. Reprod.* 64 (1), 148–156. doi:10.1095/biolreprod64.1.148

Kim, K.-S., and Gerton, G. L. (2003). Differential Release of Soluble and Matrix Components: Evidence for Intermediate States of Secretion during Spontaneous Acrosomal Exocytosis in Mouse Sperm☆. *Developmental Biol.* 264 (1), 141–152. doi:10.1016/J.YDBIO.2003.08.006

Lamas-Toranzo, I., Hamze, J. G., Bianchi, E., Fernández-Fuertes, B., Pérez-Cerezales, S., Laguna-Barraza, R., et al. (2020). TMEM95 Is a Sperm Membrane Protein Essential for Mammalian Fertilization. *eLife* 9, 1–18. doi:10.7554/eLife.53913

L. Zeng, G. (2012). A Filtered Backprojection Algorithm with Characteristics of the Iterative Landweber Algorithm. *Med. Phys.* 39 (2), 603–607. doi:10.1118/1.3673956

Marko, M., Hsieh, C., Moberlychan, W., Mannella, C. A., and Frank, J. (2006). Focused Ion Beam Milling of Vitreous Water: Prospects for an Alternative to Cryo-Ultramicrotomy of Frozen-Hydrated Biological Samples. *J. Microsc.* 222 (1), 42–47. doi:10.1111/j.1365-2818.2006.01567.x

Mastronarde, D. N. (2005). Automated Electron Microscope Tomography Using Robust Prediction of Specimen Movements. *J. Struct. Biol.* 152 (1), 36–51. doi:10.1016/j.jsb.2005.07.007

Nagae, T., Yanagimachi, R., Srivastava, P. N., and Yanagimachi, H. (1986). Acrosome Reaction in Human Spermatozoa*. *Fertil. Sterility* 45 (5), 701–707. doi:10.1016/S0015-0282(16)49344-1

Ng, C. T., and Gan, L. (2020). Investigating Eukaryotic Cells with Cryo-ET. *MBoC* 31 (2), 87–100. doi:10.1091/mbc.E18-05-0329

Nicastro, D., Schwartz, C., Pierson, J., Gaudette, R., Porter, M. E., and McIntosh, J. R. (2006). The Molecular Architecture of Axonemes Revealed by Cryoelectron Tomography. *Science* 313 (5789), 944–948. doi:10.1126/science.1128618

Noda, T., Lu, Y., Fujihara, Y., Oura, S., Koyano, T., Kobayashi, S., et al. (2020). Sperm Proteins SOF1, TMEM95, and SPACA6 Are Required for Sperm–oocyte Fusion in Mice. *Proc. Natl. Acad. Sci. USA* 117 (21), 11493–11502. doi:10.1073/pnas.1922650117

Nolan, J. P., and Hammerstedt, R. H. (1997). Regulation of Membrane Stability and the Acrosome Reaction in Mammalian Sperm. *FASEB j.* 11 (8), 670–682. doi:10.1096/fasebj.11.8.9240968

Olson, G. E., and Winfrey, V. P. (1994). Structure of Acrosomal Matrix Domains of Rabbit Sperm. *J. Struct. Biol.* 112 (1), 41–48. doi:10.1006/jsbi.1994.1005

Parrish, J. J., Susko-Parrish, J., Winer, M. A., and First, N. L. (1988). Capacitation of Bovine Sperm by Heparin1. *Biol. Reprod.* 38 (5), 1171–1180. doi:10.1095/biolreprod38.5.1171

Phillips, D. M. (1972). Substructure of the Mammalian Acrosome. *J. Ultrastruct. Res.* 38 (5–6), 591–604. doi:10.1016/0022-5320(72)90092-5

Rigort, A., Bauerlein, F. J. B., Villa, E., Eibauer, M., Laugks, T., Baumeister, W., et al. (2012). Focused Ion Beam Micromachining of Eukaryotic Cells for Cryoelectron Tomography. *Proc. Natl. Acad. Sci.* 109 (12), 4449–4454. doi:10.1073/pnas.1201333109

Russell, L., Peterson, R., and Freund, M. (1979). Direct Evidence for Formation of Hybrid Vesicles by Fusion of Plasma and Outer Acrosomal Membranes during the Acrosome Reaction in Boar Spermatozoa. *J. Exp. Zool.* 208 (1), 41–55. doi:10.1002/jez.1402080106

Satouh, Y., Inoue, N., Ikawa, M., and Okabe, M. (2012). Visualization of the Moment of Mouse Sperm-Egg Fusion and Dynamic Localization of IZUMO1. *J. Cell Sci.* 125 (21), 4985–4990. doi:10.1242/jcs.100867

Schaffer, M., Mahamid, J., Engel, B. D., Laugks, T., Baumeister, W., and Plitzko, J. M. (2017). Optimized Cryo-Focused Ion Beam Sample Preparation Aimed at *In Situ* Structural Studies of Membrane Proteins. *J. Struct. Biol.* 197 (2), 73–82. doi:10.1016/j.jsb.2016.07.010

Sosa, C. M., Pavarotti, M. A., Zanetti, M. N., Zoppino, F. C. M., De Blas, G. A., and Mayorga, L. S. (2015). Kinetics of Human Sperm Acrosomal Exocytosis. *oup* 21 (3), 244–254. doi:10.1093/molehr/gau110

Stock, C. E., and Fraser, L. R. (1987). The Acrosome Reaction in Human Sperm from Men of Proven Fertility. *Hum. Reprod.* 2 (2), 109–119. doi:10.1093/oxfordjournals.humrep.a136494

Tegunov, D., and Cramer, P. (2019). Real-time Cryo-Electron Microscopy Data Preprocessing with Warp. *Nat. Methods* 16 (11), 1146–1152. doi:10.1038/s41592-019-0580-y

Tivol, W. F., Briegel, A., and Jensen, G. J. (2008). An Improved Cryogen for Plunge Freezing. *Microsc. Microanal* 14 (5), 375–379. doi:10.1017/S1431927608080781

Travis, A. J., and Kopf, G. S. (2002). The Role of Cholesterol Efflux in Regulating the Fertilization Potential of Mammalian Spermatozoa. *J. Clin. Invest.* 110 (6), 731–736. doi:10.1172/JCI1639210.1172/jci0216392

Tsai, P.-S., Garcia-Gil, N., van Haeften, T., and Gadella, B. M. (2010). How Pig Sperm Prepares to Fertilize: Stable Acrosome Docking to the Plasma Membrane. *PLoS ONE* 5 (6), e11204. doi:10.1371/journal.pone.0011204

Tsai, P.-S., Tsai, P.-S., De Vries, K. J., Tsai, P.-S., De Vries, K. J., De Boer-Brouwer, M., et al. (2007). Syntaxin and VAMP Association with Lipid Rafts Depends on Cholesterol Depletion in Capacitating Sperm Cells. *Mol. Membr. Biol.* 24 (4), 313–324. doi:10.1080/09687860701228692

Wolff, G., Limpens, R. W. A. L., Zheng, S., Snijder, E. J., Agard, D. A., Koster, A. J., et al. (2019). Mind the gap: Micro-expansion Joints Drastically Decrease the Bending of FIB-Milled Cryo-Lamellae. *J. Struct. Biol.* 208 (3), 107389. doi:10.1016/j.jsb.2019.09.006

Yanagimachi, R. (1981). "Mechanisms of Fertilization in Mammals," in *Fertilization and Embryonic Development* in Vitro. Editors L. Mastroianni and J. D. Biggers (Boston, MA: Springer), 81–182. doi:10.1007/978-1-4684-4016-4_6

Yudin, A. I., Gottlieb, W., and Meizel, S. (1988). Ultrastructural Studies of the Early Events of the Human Sperm Acrosome Reaction as Initiated by Human Follicular Fluid. *Gamete Res.* 20 (1), 11–24. doi:10.1002/mrd.1120200103

Zanetti, N., and Mayorga, L. S. (2009). Acrosomal Swelling and Membrane Docking Are Required for Hybrid Vesicle Formation during the Human Sperm Acrosome Reaction1. *oup* 81 (2), 396–405. doi:10.1095/biolreprod.109.076166

Conflict of Interest: The authors declare that the research was conducted in the absence of any commercial or financial relationships that could be construed as a potential conflict of interest.

Publisher's Note: All claims expressed in this article are solely those of the authors and do not necessarily represent those of their affiliated organizations, or those of the publisher, the editors and the reviewers. Any product that may be evaluated in this article, or claim that may be made by its manufacturer, is not guaranteed or endorsed by the publisher.